Pure appl. geophys.
DOI 10.1007/s00024-009-0518-x

Pure and Applied Geophysics

The Energetics of Cataclasis Based on Breakage Mechanics

Giang D. Nguyen and Itai Einav

Abstract—We develop a constitutive model for rocks that are constituted from brittle particles, based on the theory of breakage mechanics. The model connects between the energetics and the micromechanics that drive the process of confined comminution. Given this ability, our model not only describes the entire stress-strain response of the material, but also connects this response to predicting the evolution of the grain size distribution. The latter fact enables us to quantify how the permeability reduces within cataclasite zones, in relation to aspects of grain crushing. Finally, our paper focuses on setting a framework for quantifying how the energy budget of earthquakes is expensed in relation to dissipation events in cataclasis. We specifically distinguish between the dissipation directly from the creation of new surface area, which causes further breakage dissipation from the redistribution of locked-in stored energy from surrounding particles, dissipations from friction and from the configurational reorganisation of particles.

Key words: Cataclasis, fault gouge, breakage, permeability, energy balance, fracture energy.

1. Introduction

The stability of fault gouges holds the key to understanding earthquake dynamics (e.g., Marone *et al.*, 1990; Scholz, 1990; Ben-Zion and Sammis, 2003), and the associated release of energy (e.g., Sleep and Blanpied, 1992; Reches and Dewers, 2005). Fault gouges evolve in high pressure or even ultrahigh-pressure environments of cataclasis (e.g., Morrow *et al.*, 1981; Lund and Austrheim, 2003), commonly because of the severe motion of the lithospheric plate boundaries. In fault gouges, cataclastic rocks undergo lifecycles of healing and granulation (Marone *et al.*, 1995; Olsen *et al.*, 1998; Renard *et al.*, 2000; Tenthorey *et al.*, 2003; Heilbronner and Keulen, 2006; Ben-Zion, 2008). During the granulation stage the parent rocks initially disintegrate into the product of granular minerals, which may then be furthered crushed during the tectonic slip. The grain size distribution (*gsd*) is therefore an evolving property during the slip, which starts from a healed agglomerated rock mass and becomes attracted towards an ultimate grading that is often found (or conveniently assumed) to be fractal, complying both self-similarity and power-law scaling (Sammis *et al.*, 1986; Steacy and Sammis, 1991; An and Sammis, 1994). Experiments show that this continuous shift of the *gsd* towards

School of Civil Engineering J05, The University of Sydney, Sydney, NSW 2006, Australia.
E-mail: i.einav@civil.usyd.edu.au

smaller-sized particles governs the inelastic behaviour of the material. Dilation shear bands are observed in geomaterials at low confining pressure, however in high-pressure cataclastic shear, the material contracts because it is easier for the particles to crush than dilate; instead shear-enhanced compaction bands tend to form (e.g., MANDL *et al.*, 1977; SCHULTZ and SIDDHARTHAN, 2005; AYDIN *et al.*, 2006). This contraction effect is important to quantify as it may result in the build-up of internal pore pressures, reduction of effective pressures and possibly the trigger of fault instability (BEELER *et al.*, 1996; ZHANG and TULLIS, 1998; GUO and MORGAN, 2007).

Cataclasis is a severe tectonic process that includes the distortion, sliding, fracture and bending of sublayers. These mechanisms dissipate energy, which controls the amount of energy release. A prevailing assumption was made that in cataclasis grain-crushing is a negligible contributor, compared to the earthquake energy budget in general and frictional shear dissipation in specific (e.g. OLGAARD and BRACE, 1983; SCHOLZ, 1990; CHESTER *et al.*, 2005). We examine the energy balance issue from a mechanistic direction. In particular, we uniquely distinguish between two seemingly similar, but different entities: the dissipation from grain crushing, or as we call it 'breakage dissipation', and from the creation of new surface area, or 'surface area dissipation'. Breakage dissipation embodies the surface area dissipation, but also the dissipation to the surrounding from the redistribution of locked-in strain energy; this latter factor, in fact, appears more significant in value, though triggered by the same grain crushing event. Using a mechanical analog, a simple demonstration of this point is given in the Appendix.

A more general account of these issues of cataclasis is explored here however primarily using the theory of 'breakage mechanics' (EINAV, 2007a,b). While the breakage mechanics theory bears striking links to fracture mechanics (EINAV, 2007c), it is directly linked to the statistics of the *gsd*. The introduction of the concept of Breakage, B, allows the development of a new hierarchy of constitutive models, which for the first time can consistently account for the effect of the *gsd* as a predictable constitutive variable. An alternative understanding of energy release is therefore motivated herein by advancing this hierarchical development for the study of cataclasis problems, through the establishment of a realistic and useful model version. The model connects between the energetics and the micromechanics that drive the process of confined comminution.

Models based on damage mechanics have been used extensively (e.g., LYAKHOVSKY *et al.*, 1997; RICARD and BERCOVICI, 2003; HAMIEL *et al.*, 2004) to study the mechanical behaviour of rocks and the formation of shear bands at appropriate scales (e.g. Fig. 1). In these models, the use of a scalar damage variable may characterize the underlying evolution of the micro-structures, if the representative volume can be considered large enough to allow viewing the distribution of the internal flaws as homogeneous (HAMIEL *et al.*, 2004). On the other hand the use of Critical State Soil Mechanics (CSSM) has also been adopted (e.g. SHAH, 1997; CUSS *et al.*, 2003; SHELDON *et al.*, 2006) to analyse the mechanical and permeability evolution of faulted rocks. Our study focuses on the material within the cataclasite layer (Fig. 1), where the emergence of granular-like behaviour is expected. Therefore, rather than stretching the limits of CSSM, by

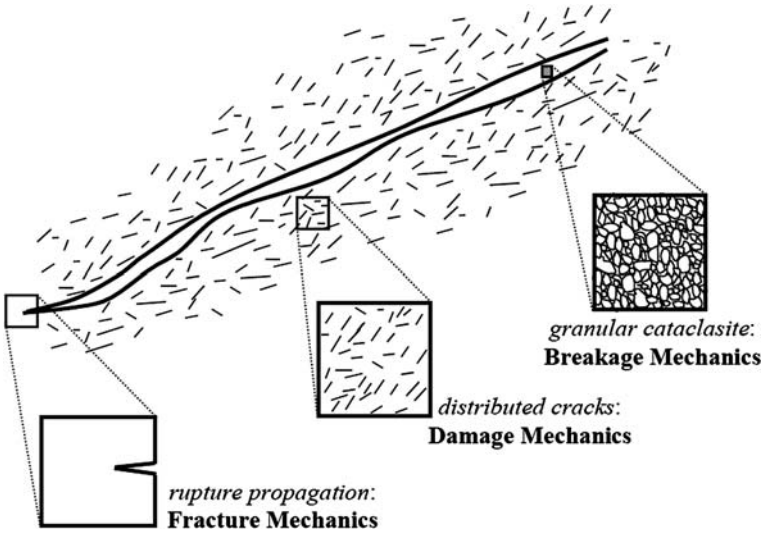

Figure 1
Fault gouge, cataclasis and the scope of breakage mechanics.

introducing *ad hoc* equations and parameters, we attack the problem from a new and rather more physical direction, illustrating how breakage mechanics allows prediction of the permeability reduction in a natural way by tracking the *gsd*. The constitutive behaviour and the particular fabric formation in the deformation bands of geomaterials depend on the loading paths (Schultz and Siddharthan, 2005; Aydin *et al.*, 2006). For that purpose our predictions will cover a wide range of loading conditions, without adjusting a few physically meaningful parameters used in breakage mechanics (Einav, 2007b,c). Our mathematical advances of the model concentrate on developing Hertzian-like (hyper)elastic stiffness matrix and the related stored free energy potential. We then introduce this into the model of the breakage mechanics formulation, and quantify the energetics in cataclasis.

2. A Model Based on Breakage Mechanics

2.1. Fundamental Constitutive Equations

The evolution of *gsd* governs the mechanical properties of crushable geomaterials in shear-enhanced cataclastic bands (e.g., Wong *et al.*, 1997; Zhu and Wong, 1997; Olsson, 1999; Schultz and Siddharthan, 2005). An ideal constitutive model for cataclastic materials should be able to predict the evolution of the *gsd*, which will guide the predictions of the mechanical behaviour. This is an essential feature that, at least until recently, has not been addressed appropriately.

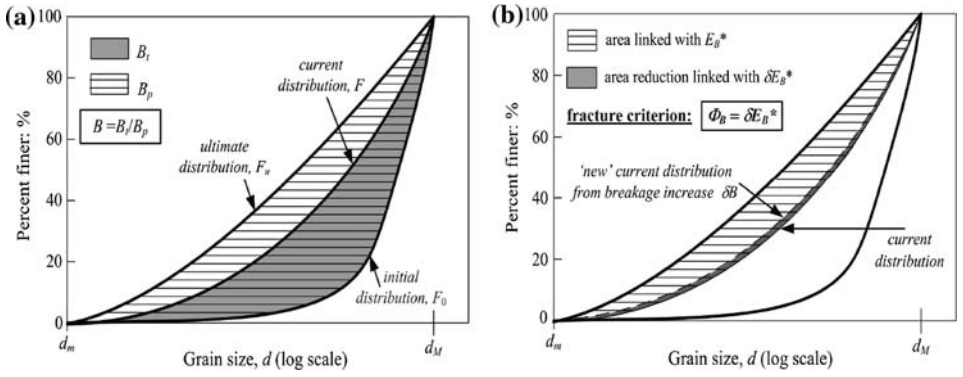

Figure 2

The breakage measurement and evolution law (EINAV, 2007a,c). The left figure (a) portrays the measurable definition of breakage. The right diagram (b) presents the breakage propagation criterion for granular materials. Φ_B is the breakage dissipation, denoting the energy consumption from incremental increase of breakage. δE_B^* is the incremental reduction in the residual breakage energy.

The formulation of a thermodynamically consistent constitutive model that is able to predict the evolving *gsd* in granular materials has been proposed by EINAV (2007a,b). The theory allows tracking the relative distance of the current (evolving) *gsd* ($p(d)$; d is the grain diameter) from the initial ($p_0(d)$) and ultimate ($p_u(d)$) *gsd*'s via the use of a macroscopic internal variable B called 'breakage' (see Fig. 2a):

$$p(d) = (1 - B)p_0(d) + Bp_u(d). \tag{1}$$

It was therefore termed "continuum breakage mechanics", in analogy with the term "continuum damage mechanics" in solid mechanics. In turn, predicting the breakage allows estimating the current *gsd*, given assumed initial and ultimate *gsd*'s. Breakage is therefore a measurable state quantity that could be directly deduced by measuring the *gsd*.

In thermodynamic context, the form of the Helmholtz energy potential for breakage mechanics models is obtained from a statistical homogenization process, taking into account the effects of the *gsd* on the macroscopic behaviour of the material model (EINAV, 2007a):

$$\Psi = (1 - \vartheta B)\psi_r(\boldsymbol{\varepsilon}), \tag{2}$$

where $\psi_r(\boldsymbol{\varepsilon})$ is expressed in terms of the total strain tensor $\boldsymbol{\varepsilon}$ and represents the elastic strain energy in a reference grain size

$$d_r = \sqrt{\int_{d_m}^{d_M} d^2 p_0(d)\, \mathrm{d}d} = \left\langle d^2 \right\rangle_0^{1/2}. \tag{3}$$

It can be seen from Eq. (2) that the reference elastic strain energy $\psi_r(\boldsymbol{\varepsilon})$ represents the virgin elastic strain energy before crushing commences. The special form of the reference particle size d_r was obtained via the execution of statistical

homogenization, averaging the elastic strain energy stored in the various fraction sizes. The proximity index property ϑ in (2) is a result of the same statistical homogenization procedure:

$$\vartheta = 1 - \left\langle d^2 \right\rangle_u \Big/ \left\langle d^2 \right\rangle_0 \tag{4}$$

and can be seen as a "distance" measure between the initial and ultimate *gsd*'s, with $\left\langle d^2 \right\rangle_u$ and $\left\langle d^2 \right\rangle_0$ being the second order moments of the ultimate and initial grain size distribution functions (by mass).

From (2), the energy conjugated to the breakage variable is defined as:

$$E_B = -\frac{\partial \Psi}{\partial B} = -\vartheta \psi_r(\boldsymbol{\varepsilon}). \tag{5}$$

The crushing of particles creates new surface areas which leads to energy release via the dissipation (termed Φ_B) of the breakage process. It was proposed that the breakage dissipation is driven by the loss of strain energy in the particles, as schematically portrayed in Figure 2b and mathematically expressed by:

$$\Phi_B = \delta E_B^*, \tag{6}$$

where

$$E_B^* = (1 - B) E_B \tag{7}$$

is the residual breakage energy, that has the physical meaning of the *available* energy in the system for the crushing process (Einav, 2007a). Eq. (6) is an important feature in exploring the relationship between the input energy (e.g., from an earthquake or a mechanical process) and the energy released due to crushing of particles.

The yield criterion, which signifies the onset and then governs the evolution of breakage can be readily worked out from (6) and (7) (Einav, 2007c):

$$y_B = (1 - B)^2 E_B - E_c = 0, \tag{8a}$$

where E_c, a constant arising from the derivation process and termed the critical breakage energy, is an energy constant (with stress units) of the granular material. Later in section 2.3 (see eqs. (26) and (34)) we can see that E_c in the formula for critical pressure has a role similar to Griffith's fracture energy constant G_c (Griffith, 1921) in the critical stress formula in fracture mechanics. However, their physical interpretations are different. The introduction of the yield criterion required the specification of the analysis to rate-independent processes, suggesting that during dissipation $E_B = \partial \Phi_B / \partial B$, and $\Phi_B = (\partial \Phi_B / \partial B) \delta B$.

In addition, a link between the breakage measure and the changes of the specific surface areas was derived (Einav, 2007c), suggesting a deeper look at the model from the viewpoint of fracture mechanics:

$$B = \frac{S - S_0}{S_u - S_0}, \tag{8b}$$

where the initial and ultimate specific surface areas (the averaged surface area of particles divided by their volumes; unit of 1/length, e.g. 1/mm) are defined respectively as $S_0 = 6\langle d^{-1}\rangle_0$ and $S_u = 6\langle d^{-1}\rangle_u$. This relationship between B and S, as two dependent internal variables of a thermo-mechanical process, suggests that the breakage dissipation Φ_B can be viewed in terms of the current specific surface area S and its associated energy $E_S = \partial\Psi/\partial S = E_B(S_u - S_0)$:

$$\Phi_B = E_B \delta B = E_S \delta S, \tag{9}$$

where E_B has the unit of energy (e.g., N/mm^2), and E_S unit of energy times length (e.g., N/mm^2*mm). The last relation resembles the increment of non-negative entropy production, as defined by Rice (1978). The property E_S is parallel to specific surface energy γ as in Griffith's analysis. However, we note that breakage mechanics accounts for the redistribution of the elastic stored energy in the particles, as we will further discuss in the following.

2.2. *Model Formulation*

Based on the above fundamentals and earlier developments in Einav (2007b,c), our current formulation will account for the coupling between the release of surface energy and other dissipative mechanisms, namely the dissipations due to frictional shear and the reorganisation of the granular ensemble following crushing. A triaxial exposition is used in the formulation, for which standard notations in soil mechanics are employed as follows: Mean effective stress p (positive in compression), shear stress q, total volumetric strain ε_v and elastic volumetric strain ε_v^e (positive in contraction), total shear strain ε_s and elastic shear strain ε_s^e. The Helmholtz free energy potential Ψ and dissipation potential Φ, from which all other constitutive equations are derived, take the following general forms:

$$\Psi = (1 - \vartheta B)\left[\psi_v\left(\varepsilon_v^e\right) + \psi_s\left(\varepsilon_v^e, \varepsilon_s^e\right)\right], \tag{10}$$

$$\Phi = \sqrt{\Phi_B^2 + \Phi_p^{v^2} + \Phi_p^{s^2}}. \tag{11}$$

Use of Ψ in its general form (10) allows the incorporation of both pressure-independent and pressure-dependent features into the elastic behaviour of the material. Functions ψ_v and ψ_s in (10) govern the elastic volumetric and shear behaviours of the model, and represent the 'unbroken' stored energy in a reference particle size d_r; this paper places particular attention on refining the particular structures of ψ_v and ψ_s.

In this regard breakage can be experimentally measured with reference to Figure 2a. The dissipation potential Φ comprises three parts corresponding to breakage dissipation Φ_B, plastic volumetric dissipation Φ_p^v and plastic shear dissipation Φ_p^s :

$$\Phi_B = \frac{\sqrt{2E_B E_c}}{(1-B)}\delta B, \tag{12}$$

$$\Phi_p^v = \frac{p}{(1-B)}\sqrt{\frac{2E_c}{E_B}}\delta\varepsilon_v^p, \tag{13}$$

$$\Phi_p^s = Mp\left|\delta\varepsilon_s^p\right|, \tag{14}$$

where Φ_B was derived from the energy balanced criterion of Figure 2b, Φ_p^v was obtained by applying the understanding that in isotropic compression particle reorganisation is only passive to breakage, and Φ_p^s was derived by consulting with Coulomb's friction law. In the above equations $M = q_u/p_u$ is the ratio between the ultimate shear stress q_u and ultimate volumetric stress p_u at failure (i.e., related to the ultimate mobilised friction angle); finally, ε_v^p and ε_s^p are the volumetric and shear plastic strains. Note that the above model does not involve the coupling angle ω, as explored by Einav (2007b); instead, this angle is conveniently taken as 45°. It will be shown later that this simplification results in the same relationship between the incremental plastic volumetric and shear strains as in the modified Cam clay model (Roscoe and Schofield, 1963).

Via Eqns. (11)–(14), we identify three components of dissipation: frictional dissipation Φ_p^s, dissipation from the configurational reorganisation of particles Φ_p^v, and from breakage Φ_B. Here, the 'reorganisation dissipation' Φ_p^v is simply represented by the volumetric plastic dissipation, which relates to the increasing capacity of the particles to organise within fixed volumes, since the sub-elements are growing in numbers, i.e., representing dissipation in the sense of increasing configurational entropy via changing granular compactivity (Edwards and Grinev, 2001). We note that while the breakage dissipation Φ_B can be calculated alternatively in relation to the increasing specific surface area (Einav, 2007c), its value does not correspond entirely to 'surface area dissipation'. Most of the breakage dissipation arises from the redistribution of locked-in stored energy. An analog that portrays this point is given in the Appendix.

The constitutive equations can be defined as the derivatives of the potentials as follows:

$$p = \frac{\partial\Psi}{\partial\varepsilon_v^e} = (1-\vartheta B)\left(\frac{\partial\psi_v}{\partial\varepsilon_v^e} + \frac{\partial\psi_s}{\partial\varepsilon_v^e}\right), \tag{15}$$

$$q = \frac{\partial\Psi}{\partial\varepsilon_s^e} = (1-\vartheta B)\frac{\partial\psi_s}{\partial\varepsilon_s^e} \tag{16}$$

$$E_B = -\frac{\partial\Psi}{\partial B} = \vartheta\left[\psi_v\left(\varepsilon_v^e\right) + \psi_s\left(\varepsilon_v^e, \varepsilon_s^e\right)\right]. \tag{17}$$

The yield function y^* in dissipative stress space is obtained as a result of the degenerate Legendre transformation of the dissipation potential (11):

$$y^* = \left(\frac{E_B}{\partial \Phi_B / \partial \delta B}\right)^2 + \left(\frac{p}{\partial \Phi_p^v \Big/ \partial \delta \varepsilon_v^p}\right)^2 + \left(\frac{q}{\partial \Phi_p^s \Big/ \partial \delta \varepsilon_s^p}\right)^2 - 1 \leq 0 \tag{18}$$

with the following flow rules ($\delta\lambda$ is a common non-negative multiplier):

$$\delta B = \delta\lambda \frac{\partial y^*}{\partial E_B} = 2\delta\lambda \frac{E_B}{\left(\partial \Phi_B / \partial \delta B\right)^2} = 2\delta\lambda \frac{(1-B)^2}{2E_c}, \tag{19}$$

$$\delta \varepsilon_v^p = \delta\lambda \frac{\partial y^*}{\partial p} = 2\delta\lambda \frac{p}{\left(\partial \Phi_p^v \Big/ \partial \delta \varepsilon_v^p\right)^2} = 2\delta\lambda \frac{E_B (1-B)^2}{2pE_c}, \tag{20}$$

$$\delta \varepsilon_s^p = \delta\lambda \frac{\partial y^*}{\partial q} = 2\delta\lambda \frac{q}{\left(\partial \Phi_p^s \Big/ \partial \delta \varepsilon_s^p\right)^2} = 2\delta\lambda \frac{q}{(Mp)^2}. \tag{21}$$

Using (12)–(14), y^* can be replaced by the mixed breakage/yield function:

$$y_{mix} = \frac{E_B (1-B)^2}{E_c} + \left(\frac{q}{Mp}\right)^2 - 1 \leq 0. \tag{22}$$

It should be noted that in principle y_{mix} can be further rewritten, fully in terms of triaxial stresses p and q, and the breakage B, provided the explicit expressions of ε_v^e and ε_s^e in terms of p and q are obtained from (15) and (16). In this case, we will redesignate the yield function again by replacing the notation y_{mix} with y. Non-associated flow rules for breakage and plastic shear strain are a direct consequence of the derivation procedure and no assumption relative to the existence of a plasticity/breakage potential is required.

Using (20), (21) and the yield condition (22), the ratio between the incremental plastic volumetric and shear strains is obtained as:

$$\frac{\delta \varepsilon_v^p}{\delta \varepsilon_s^p} = \frac{M^2 - \eta^2}{2\eta} \quad \text{with} \quad \eta = \frac{q}{p}.$$

Perhaps attractive, in structure the above ratio coincides with that of the modified Cam clay model (Roscoe and Schofield, 1963), but the current model is obviously different. On the other hand, this result motivates us to take ω as 45°, as discussed earlier.

2.3. *Hierarchy in Model Development*

It is interesting to note that in breakage mechanics the elastic properties directly affect post-yield behaviour. This is due to the presence of the energy-like quantity E_B in the mixed breakage/yield function (22). E_B is a function of the elastic stored energy, and governs the rate of dissipation during the crushing process. Consequently, the hardening of the material during comminution is directly driven by the competition between E_B and

$(1-B)^2$: as B grows towards unity, E_B must increase to balance the equality in eq. (22). Since E_B depends on the elastic strains via eq. (17), changing the elastic law will directly change the model response in the inelastic regime. Subsequently, improving the model behaviour in the elastic regime may automatically result in positive improvements in the inelastic regime. We believe that this aspect is a genuine step ahead, which allows us to be more economical in introducing model parameters, all by applying first principles. The best example is our capability to eliminate parameters such as the so-called normally-consolidated compression index λ in CSSM, which bears no direct physical meaning but is purely a fitting parameter. This economy in model parameters is discussed in length by Einav (2007d), highlighting that the modelling of crushable granular materials using CSSM should require at least four additional *adhoc* parameters (slope λ of the isotropic hardening compression line, specific volume parameter N, and two additional parameters to span the range of λ and N) to achieve the same level of detail.

In the following we extend the hierarchy of Einav's breakage model by refining the structure of the reference stored energy functions ψ_v and ψ_s. We start by illustrating the effects of using linear elasticity, but then replace this by developing a nonlinear hyperelastic Hertzian-like model of ψ_v and ψ_s. Both models require only 4 physical parameters, however applying the more realistic elastic law clearly improves the predictions.

2.3.1 Use of linear isotropic elasticity. Linear elasticity is the simplest elastic law possible, which requires two constant parameters, e.g., the bulk and shear moduli K and G. For this purpose, ψ_v and ψ_s are defined as follows:

$$\psi_v = \frac{1}{2} K \varepsilon_v^{e^2}, \tag{23}$$

$$\psi_s = \frac{3}{2} G \varepsilon_s^{e^2}. \tag{24}$$

In this case, the breakage/yield surface in true triaxial stress space is written as:

$$y = \frac{\vartheta}{2E_c}\left(\frac{1-B}{1-\vartheta B}\right)^2\left(\frac{p^2}{K}+\frac{q^2}{3G}\right)+\left(\frac{q}{Mp}\right)^2-1\leq 0. \tag{25}$$

Solving Eq. (25) for $q = 0$ and $B = 0$, the crushing pressure p_c in isotropic compression is given by:

$$p_c = \sqrt{\frac{2KE_c}{\vartheta}}. \tag{26}$$

As discussed by Einav (2000c), this relation bears a striking relation to Griffith's criterion in fracture mechanics. Figure 3a shows the breakage/yield surface and its evolution in triaxial stress space. This simple model was motivated by Einav (2007d) as a "student model" to illustrate certain features of breakage mechanics models. In the next section

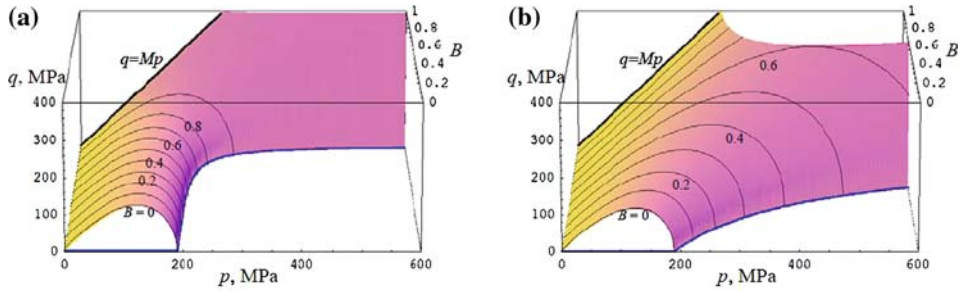

Figure 3
Yield/breakage surface in p-q-B space, using: (a) linear elasticity (Einav, 2007d), and (b) pressure-dependent elasticity. While the $B = 0$ projection planes are quite similar, the projection planes along progressing B values are of different sizes. (To generate these plots, parameters were taken in relation to the Adamswiller sandstone, as listed in Table 1).

we further advance the model, slightly increasing the complexity, but not the number of parameters.

2.3.2 Use of pressure dependent elasticity. Enhancement to the model response can be made by developing appropriate nonlinear (hyper)elastic terms ψ_v and ψ_s, which account for pressure-dependent bulk and shear moduli. From eqs. (15) and (16), the incremental stress-strain behaviour of the model in the elastic regime ($\delta B = 0$) is given as $\{\delta p, \delta q\}^T = (1 - \vartheta B)\mathbf{D}\{\delta\varepsilon_v^e, \delta\varepsilon_s^e\}^T$, where $\mathbf{D}$ is the elastic tangent stiffness matrix in triaxial stress space, defined by:

$$\mathbf{D} = \begin{bmatrix} \left(\dfrac{\partial^2\psi_v}{\partial\varepsilon_v^{e^2}} + \dfrac{\partial^2\psi_s}{\partial\varepsilon_v^{e^2}}\right) & \dfrac{\partial^2\psi_s}{\partial\varepsilon_s^e\partial\varepsilon_v^e} \\ \dfrac{\partial^2\psi_s}{\partial\varepsilon_s^e\partial\varepsilon_v^e} & \dfrac{\partial^2\psi_s}{\partial\varepsilon_s^{e^2}} \end{bmatrix}. \tag{27}$$

Therefore the general form of ψ_v and ψ_s introduces both the presence of cross-coupling and additional bulk terms in the elastic stiffness tensor. These terms are absent in the linear elastic model, but present in non-linear elastic models, and correspond to stress-induced anisotropy and elastic dilation, which is experimentally observed in granular materials (e.g., LoPresti and O'Neill, 1991; Hoque and Tatsuoka, 1998). Similar understanding has been motivated in previous studies of the (hyper)elasticity of granular materials (Zytynski *et al.*, 1978; Houlsby, 1985; Einav and Puzrin, 2004; Houlsby *et al.*, 2005).

In the development of the pressure-dependent model, we first assume the function ψ_v to describe the behaviour of the model in isotropic compression, which is then used to guide the determination of function ψ_s, thus revealing the appropriate stress-induced cross anisotropy terms. The following form of ψ_v is adopted from Einav (2007b):

$$\psi_v = p_r \frac{\left[\xi\left(\varepsilon_v^e\right)/p_r\right]^{2-m}}{\bar{K}(2-m)}, \tag{28}$$

where $\xi\left(\varepsilon_v^e\right) = p_r \sqrt[1-m]{\bar{K}(1-m)\left(\varepsilon_v^e - \varepsilon_{vr}\right) + 1}$ and p_r is defined as a reference pressure conveniently taken as 1 kPa; $m = 0.5$ (for Hertzian contact), $\bar{K}$ and $\bar{G}$ are nondimensional material constants, which replace the dimensional K and G, and ε_{vr} the initial volumetric strain dependent on the maximum $e_{\max}$ and initial e_0 void ratios of the sample (Einav, 2007d): $\varepsilon_{vr} = -\log((1+e_0)/(1+e_{\max}))$. Since experimental data for $e_{\max}$ are not available in our comparisons, for simplicity, we take the reference strain as $\varepsilon_{vr} = 0$.

The reference shear stored energy ψ_s can be conveniently assumed to decompose into two multiplicative parts, with the shear modulus being pressure-dependent:

$$\psi_s = \frac{3}{2} p_r \bar{G} \left[\frac{\xi\left(\varepsilon_v^e\right)}{p_r}\right]^m \varepsilon_s^{e^2}. \tag{29}$$

The stress-dependent elastic stiffness matrix (27) in this case ($m = 0.5$) becomes:

$$\mathbf{D} = \begin{bmatrix} p_r \bar{K} A & \frac{q\bar{K}}{2A} \\ \frac{q\bar{K}}{2A} & 3p_r \bar{G} A \end{bmatrix}, \tag{30}$$

where $A = \sqrt{\xi/p_r} = \bar{K}\varepsilon_v^e/2 + 1$ is purely stress-dependent, obtained by replacing the volumetric elastic strain by solving the system of eqs. (15)–(16) in terms of triaxial stresses p and q:

$$A = \sqrt{\frac{p^*}{2} + \sqrt{\left(\frac{p^*}{2}\right)^2 - \frac{1}{12}\frac{\bar{K}}{\bar{G}} q^{*2}}}, \tag{31}$$

where $p^* = p/p_r$ and $q^* = q/p_r$. Along the isotropic compression axis ($q = 0$), the apparent shear and bulk modulii are given as:

$$K = \bar{K}\sqrt{p^*} \quad \text{and} \quad G = \bar{G}\sqrt{p^*}. \tag{32}$$

Using (28), (29) and (31), the breakage/yield surface can be rewritten in terms of triaxial stresses as:

$$y = \vartheta \left[\frac{2p_r A^3}{3\bar{K}} + \frac{q^2}{6p_r \bar{G} A (1 - \vartheta B)^2}\right] \frac{(1-B)^2}{E_c} + \left(\frac{q}{Mp}\right)^2 - 1 \leq 0. \tag{33}$$

In this case, the crushing pressure p_c in isotropic compression becomes:

$$p_c = p_r \left(\frac{3\bar{K}E_c}{2p_r\vartheta}\right)^{2/3} \tag{34}$$

corresponding to a relation given by Einav (2007c), though here completed through eq. (33). The effects of change in elastic behaviour on the shape of yield/breakage surface can be seen in Figure 3. Along with the difference observed in the evolution of the breakage/yield surface (Fig. 3b) with increasing breakage, compared to the case of linear isotropic elasticity (Fig. 3a), the response of the model is greatly improved, as we will demonstrate in the next sections.

The use of pressure-dependent (hyper)elasticity requires the elimination of instability issues, even in elastic regime. This is due to the presence of cross-coupling terms in the elastic stiffness matrix (Houlsby, 1985; Borja *et al.*, 1997; Einav and Puzrin, 2004; Houlsby *et al.*, 2005). Using (22), the stability condition $\det(\mathbf{D}) = 0$ results in:

$$\eta = \frac{q}{p} = \sqrt{\frac{3\bar{G}}{2m\bar{K}}}. \tag{35}$$

It can be shown that the above expression coincides with the expression for the maximum attainable stress ratio $\eta_{\max}$, which represents the tangent of all stress curves in elastic undrained loading. Since the complete breakage mechanics model response is bounded by the friction law $q = Mp$ (see eq. (14) and Fig. 3), it seems reasonable to restrict the choice of the parameters $\bar{G}$ and $\bar{K}$ via:

$$\frac{\bar{G}}{\bar{K}} > \frac{2mM^2}{3} = \frac{M^2}{3} (\text{for } m = 0.5). \tag{36}$$

Combining the two alternative forms of ψ_v and ψ_s with the general formulation structure completes the representation of two models.

2.4. Model Parameters

Besides the two parameters that determine the elastic behaviour (G and K with unit of stress; or $\bar{G}$ and $\bar{K}$ without a unit), which can be determined based on the stress-strain behaviour of the material in elastic regime, the model depends on only two additional parameters (E_c and M), both of which possess physical meaning. Additionally, the model behaviour also depends on the criticality proximity index property (i.e., not a parameter) $\vartheta = 1 - \langle d^2 \rangle_u / \langle d^2 \rangle_0$ (Einav, 2007a). The initial *gsd* can most often be assumed comfortably, if not by using one of the various sieving techniques, by using one of the image analysis techniques. The ultimate *gsd* can often be assumed fractal, with a fractal dimension 2.5–2.8 (Sammis *et al.*, 1986), although in pathological cases it may be different (Einav, 2007a).

The critical breakage energy E_c, which represents the elastic strain energy per unit volume stored in the material before crushing commences and governs the activation of the grain breaking process in the model, may be determined via a single isotropic compression test (eqs. (26) and (34)). In particular, the limiting breakage/yield

pressure p_c in isotropic compression is directly related to E_c, through the expression of the yield condition (22) in the absence of the triaxial shear stress q. It is noted that E_c only decides the onset but not the evolution of the dissipative process, which is in fact driven by the breakage energy E_B. The total dissipation can be determined by integrating the explicitly defined dissipation potential (eq. (11); see also section 5.1).

The last parameter is the slope M in (22), which is in fact the ratio between the triaxial shear stress q and the pressure p at ultimate critical state conditions. This parameter relates to the mobilised friction angle of the material.

In brief, only four parameters: G (or $\bar{G}$), K or $(\bar{K})$, E_c, and M are needed to complete the definition of the model and its behaviour in both elastic and inelastic regimes.

3. *Permeability Reduction*

The permeability in cataclasite zones tends to reduce, both from volumetric changes and the increasing surface area of the particles, which can thereafter act as a permeability barrier for the adjacent flow regime (Caine *et al.*, 1996; Evans *et al.*, 1997; Tenthorey *et al.*, 2003). This factor is extremely important since the changes to the flow regimes may affect the surrounding pore fluid pressures, hence the local strengths, and overall stability of the fault during earthquake cycles (Segall and Rice, 1995; Zhang and Tullis, 1998). Experiments on the material behaviour in shear bands have indicated the importance of the *gsd* in governing the evolution of the permeability (Wong *et al.*, 1997; Zhu and Wong, 1997; Okada *et al.*, 2004), i.e., from the increasing surface area. Although constitutive models based on CSSM can be adapted, calibrated and then used for the numerical analysis of crushable geomaterials (Shah, 1997; Sheldon *et al.*, 2006), their application for predicting the associated permeability changes neglects the effect of the evolving *gsd* (e.g., in Sheldon *et al.*, 2006).

Here this problem is circumvented by adopting the merits of the breakage mechanics formulation. We follow an approach which we recently developed with Prof. Ioannis Vardoulakis, from the National Technical University of Athens, to describe the permeability reduction as related to the so-called sand production problem in the petroleum industry (Einav *et al.*, 2008). Accordingly, we first express the reduction in the cataclasis problem by applying the modified Kozeny-Carman's formula (Matyka *et al.*, 2008):

$$k = c_0 \frac{\phi^3}{T^2 S^2}, \tag{37}$$

where c_0 is a constant; $T = T(\phi)$ is the tortuosity as a function of the porosity ϕ (Matyka *et al.*, 2008); S is the specific surface area of the grains. For spherical grains, $S = 6/D_H$, and (37) can be expressed in terms of the harmonic mean grain size D_H:

$$k = \frac{c_0 \phi^3}{36T^2} D_H^2. \tag{38}$$

The harmonic mean grain size D_H is defined as:

$$\frac{1}{D_H} = \int_{D_m}^{D_M} p(D)\frac{\mathrm{d}D}{D} = (1-B)\frac{1}{D_{H0}} + B\frac{1}{D_{Hu}} \tag{39}$$

in which D_H and D_m are the maximum and minimum grain sizes, respectively. Due to the grain crushing, the *gsd* $p(D)$ is also evolving, resulting in an evolving harmonic mean grain size D_H. Using relationship (1) of breakage mechanics, we can express D_H in terms of the breakage variable B, via the second equality in (39), while D_{H0} and D_{Hu} are the initial and ultimate harmonic mean grain sizes, obtained by replacing $p(d)$ with $p_0(d)$ and $p_u(d)$, respectively, in eq. (39). The permeability reduction can now be defined as:

$$R_k = \frac{k}{k_0} = \frac{(\phi/\phi_0)^3}{(T/T_0)^2}\left(\frac{D_H}{D_{H0}}\right)^2. \tag{40}$$

As can be seen, R_k composes two different contributions from the changes in the porosity ϕ and the grain sizes.

For an ultimate *gsd*, we follow Einav (2007a), who describes an ultimate cumulative fractal grading by mass that accounts for the minimum possible grain size D_m (Kendall, 1978; Sammis and Ben-Zion, 2008):

$$F(D) = \frac{D^{3-\alpha} - D_m^{3-\alpha}}{D_M^{3-\alpha} - D_m^{3-\alpha}} \tag{41}$$

from which the ultimate *gsd*, as the probability density function, can be deduced:

$$p(D) = F'(D) = \frac{(3-\alpha)D^{2-\alpha}}{D_m^{3-\alpha} - D_m^{3-\alpha}}. \tag{42}$$

As discussed by Einav *et al*. (2008), the incorporation of the minimum possible grain size D_m in the distribution proves critical for evaluating the harmonic mean grain size D_H. Without including this factor (i.e., by taking $D_m = 0$), the harmonic mean size would always be zero (i.e., getting $D_H = 0$), implicitly suggesting unrealistically that rocks with fractal *gsd* should be impermeable.

4. Numerical Simulation of Shear Tests

The behaviour of porous sandstones under drained loading (Wong *et al.*, 1997) is numerically simulated, with the use of either linear elasticity or pressure-dependent elasticity in the constitutive model. The experimental tests were conducted on various

kinds of sandstones at different confining pressures. The breakage model described in section 2 is used here in the numerical simulation. For simplicity, we neglect the cohesive strength of the material model. Taking into account cohesion would require the incorporation of another internal variable to govern decohesion (or damage) due to material degradation. The coupling between damage and breakage within a thermo-mechanical framework will obviously broaden the capability of the model. It requires further work on the coupling effects which would inevitably increase the complexity of the model while having little effect on predicting the material behaviour under high confining pressures. This incorporation of cohesive strength therefore falls beyond the scope of this study.

In the calibration of the model parameter, the linear elasticity constants (for model 1) are determined based on the experimental data and formulae described in Wong *et al.* (1997), at lateral stress $\sigma_r = 150$ MPa for the Adamswiller sandstone and $\sigma_r = 250$ MPa for the Berea sandstone. In the case of pressure-dependent elasticity, the elastic parameters were determined to provide the best fit predictions in the elastic regime, but taking into account the stability condition (36).

Since the initial and ultimate *gsd*'s were not available in the paper by Wong *et al.* (1997), the index property ϑ for the Adamswiller sandstone is calculated as follows. From eq. (3), for an assumed initial poorly-graded material we have $\vartheta \approx 1 - \langle d^2 \rangle_u / d_M^2$. Assuming that the ultimate *gsd* is fractal, i.e., that $\langle d^2 \rangle_u = d_M^2 (3-\alpha)/(5-\alpha)$ (see Einav, 2007a), $\vartheta \approx 2/(5-\alpha)$. Using the fractal dimension $\alpha = 2.7$, which falls well inside the proposed range of 2.5–2.8 (Sammis *et al.*, 1986), we have $\vartheta \approx 0.9$. For the Berea sandstone, ϑ can be determined based on an assumed fractal dimension $\alpha = 2.7$ for the ultimate *gsd* and an initial *gsd* from another source (Sammis *et al.*, 1986), and with the ultimate *gsd* by mass accounting for the minimum grain size D_m of 1 μm (see eqs. (3) and (4) in Section 2.1). Due to the irregular shape of the experimental initial *gsd* of Berea sandstone, which leads to difficulties in calculating ϑ in breakage mechanics, an assumed initial *gsd* is used, on condition that it produces the same harmonic mean grain size D_{H0} (see eq. (39)) as that of the experimental one.

In both model cases, the energy threshold E_c is determined based on the corresponding formula for the critical breakage-pressure (see Einav, 2007c, and herein Eqs. (26) and (34)), using the same crushing pressure p_c. Since the underlying elastic behaviour is different for models 1 and 2, the values of E_c are therefore different in both cases. Table 1 summarizes the parameters for the models used. Note that besides higher stiffness (compared to that of sand) the energy-like parameter E_c for sandstones, which has the meaning of energy stored in the material before crushing, is about one to two orders of magnitude higher than that for sand (see Einav, 2007b).

A quick assessment of the parameters K or $\bar{K}$ and the corresponding E_c can be done by plotting the normal compression curve against the experimental counterpart (Fig. 4). We can see that the inelastic behaviour is greatly improved just by correcting the underlying elasticity of the model. It is stressed that this correction is done without having to introduce additional parameters as required in CSSM models for fitting

Table 1

Model parameters for sandstones

Model	Adamswiller sandstone ($\vartheta = 0.9$; $p_c = 190$ MPa)	Berea sandstone ($\vartheta = 0.6$;$p_c = 380$ MPa)
Using linear elasticity (model 1)	$G = 4710$ MPa; $K = 4608$ MPa; $M = 1.5$; $E_c = 3.53$ MPa	$G = 4637$ MPa; $K = 19109$ MPa; $M = 1.5$; $E_c = 2.27$ MPa
Using pressure-dependent elasticity (model 2)	$\bar{G} = 16500$; $\bar{K} = 22000$; $M = 1.5$; $E_c = 2.26$ MPa	$\bar{G} = 14250$; $\bar{K} = 19000$; $M = 1.5$; $E_c = 4.93$ MPa

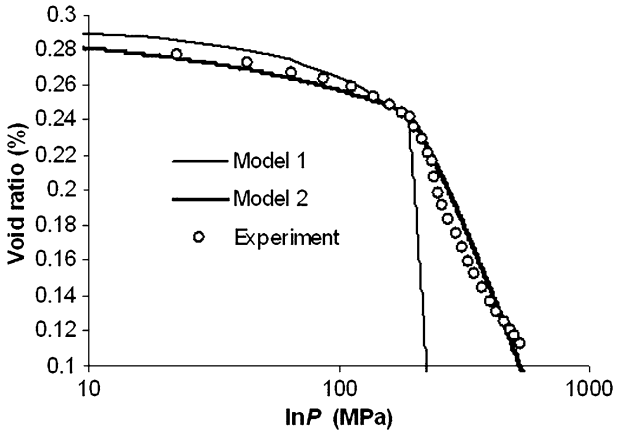

Figure 4
Normal compression curves (Adamswiller sandstone; experimental data from Wong *et al.*, 1997).

experimentally-based normal compression curves (e.g., as in Sheldon *et al.*, 2006). Model 2 of the pressure-dependent elasticity improves the numerical predictions in both pre- and post-breakage/yielding regimes.

Figure 5 shows the model and experimental yield/breakage surfaces for the Adamswiller and Berea sandstones in triaxial stress space. We remind that the evolution of the surfaces with growing B is given along a 3-D space in Figure 3 for the Adamswiller sandstone. Both brittle failure (denoted as "b" in Fig. 5) and shear-enhanced compaction (denoted as "c") regimes of the experimental initial yield/breakage surfaces are shown. Good agreements between numerical and experimental data for both kinds of sandstones can be observed in shear-enhanced compaction regime (open symbols, Fig. 5), where the model is aimed for. It is also noted here that the chosen pressure-dependent elastic parameters for the Berea sandstone lead to better prediction of the experimental surface, compared to that of the linear elastic model. In the regime of brittle failure (solid symbols, Fig. 5) the theoretical breakage surface is restricted by the critical state line $q = Mp$ and hence does not yield a perfect match with the experimental values. Continuing along the hierarchical structure of the breakage mechanics, model

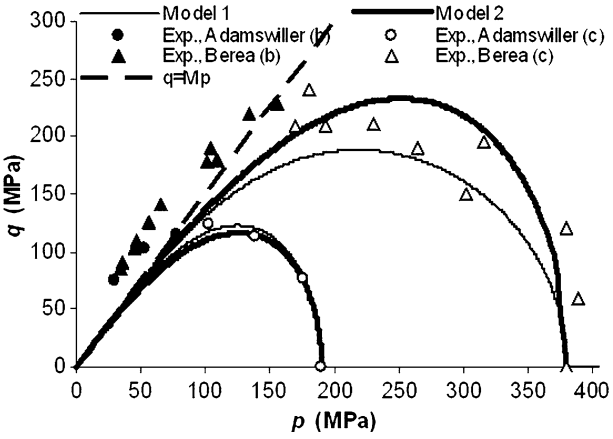

Figure 5
Yield/breakage surfaces for two kinds of sandstones (experimental data from Wong *et al.*, 1997).

derivation can enable to derive a more sophisticated model that focuses further on the behaviour above the critical state line, prior to reaching failure, but falls beyond our current aim of forming the simplest possible exposition.

The behaviour of the sandstones under different confining stress, in drained triaxial tests, is illustrated in Figure 6. The qualitative trends in the response of the material are well predicted by both models.

The experimental evolution of the porosity changes under different loading conditions (Wong *et al.*, 1997) is depicted in Figure 7. It can be seen that the model can capture rather well the trends in porosity changes. In addition the degree of matching of the models with the experimental results is improved considerably if the elastic law is taken as pressure-dependence (model 2).

For brevity, in the following we will continue with the predictions using model 2 only, as that seems to be superior. The predictions of the permeability evolution are based on the formula in Section 3 which includes changes in both porosity and grain sizes. The porosity change is illustrated in Figure 8a, agreeing very nicely with the experimental data for the Berea sandstone, considering the small number of parameters. Note, however, that the predictions of the permeability reduction rely on the dependency of the formula on the porosity. Good agreement in the first stage (before any grain crushing), where the reduction in the permeability is only due to the change in the porosity, is obtained by assuming $T \propto \phi^{-p}$ (with $p = 5$) in the modified Kozeny-Carman's formula (Matyka *et al.*, 2008), while the original formula ($T \propto 1 - \phi$) fails. A similar expression for describing the permeability reduction in fault gouges was made by Tenthorey *et al.* (2003). In post breakage/yielding, the permeability reduction curves abruptly change their slope due to the grain size reduction (i.e., the increasing specific surface area). This rapid change in the permeability is clearly portrayed via the experiments in Figure 8b,

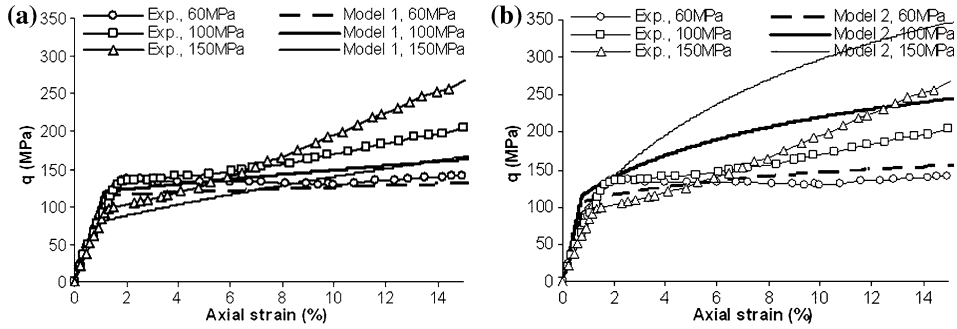

Figure 6

Stress-strain behaviour at different levels of effective lateral stress. (a): Model 1 (linear elasticity); (b): Model 2 (pressure-dependent elasticity). (Adamswiller sandstone; experimental data from Wong *et al.*, 1997).

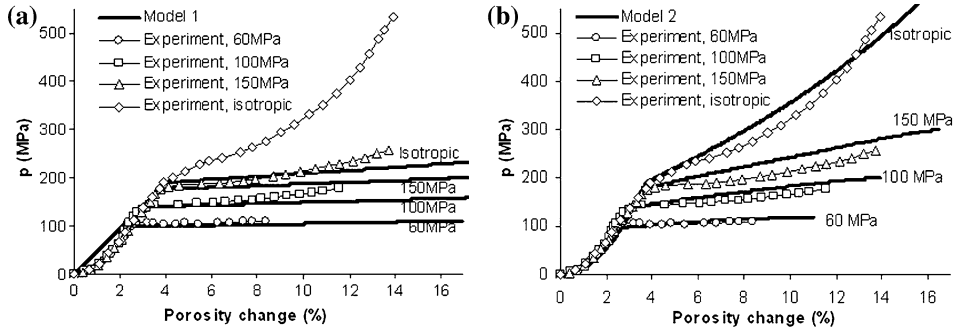

Figure 7

Porosity changes in different loading conditions. (a): Model 1); (b): Model 2. (Adamswiller sandstone; experimental data from Wong *et al.*, 1997).

against the evolving effective mean stress. The effect of grain size reduction on the permeability reduction is novel in continuum mechanics, as the theory of breakage mechanics provides the first access of continuum mechanics to modelling confined comminution.

5. *A look at energetics*

We now turn our attention to a study of the energy balance in fault gouges. We focus on the dissipation from the particulate gouge material, rather than aspects of fracture and damage mechanics, such as the scaling of fracture energy (e.g., McGarr *et al.*, 2004; Xia, 2006). There is a growing appreciation that the ratio between the dissipated surface energy and dissipated frictional energy from the gouge is a significant factor for understanding earthquake dynamics (e.g., Olgaard and Brace, 1983; Chester *et al.*,

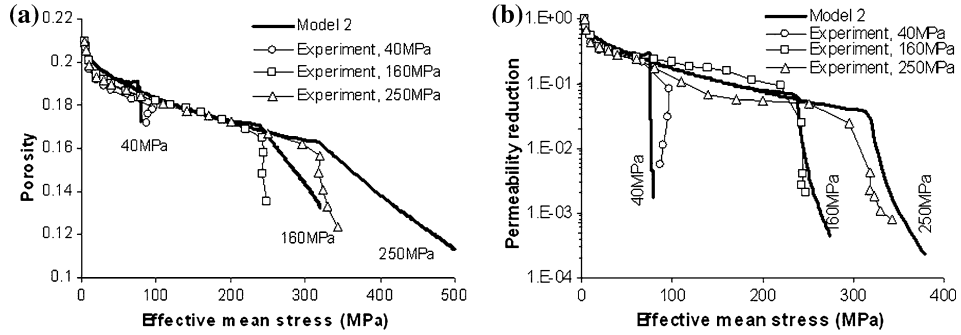

Figure 8

Porosity change and permeability reduction in drained shearing at different effective confining pressures (Berea sandstone; experimental data from Zhu and Wong, 1997). (a): Porosity change; (b): Effective mean stress – permeability reduction.

2005; Reches and Dewers, 2005; Wilson *et al.*, 2005; Pittarello *et al.*, 2008; Shi *et al.*, 2008). To examine this, we provide a rather different view based on breakage mechanics that is supported by a mechanical analog, shown in the Appendix. The breakage models in this study will be used to characterize fault gouge materials (Fig. 1), which involves the crushing of rock grains and consequently the rearrangement of fragments, which may induce severe compaction. They are not aimed at modelling the full scale fault zone, which includes both the damage zone and cataclasite layer, as seen in Figure 1. We therefore wish to classify our following results, on aspects of energy partition, to be more relevant to cataclasite layers rather than the whole fault zone. It is however noted that most of the earthquake energy consumed for creating new surface areas (more than 90%, as in Chester *et al.*, 2005) is due to the crushing of grains within the cataclasite layer.

Figure 9 illustrates the various compressive dissipative mechanisms (i.e., not representing frictional dissipation, that is pivotal in shear) in terms of a single crushing grain and its first ring of neighbours. The breakage dissipation is not only due to freeing surface energy, directly from the split of the particles, i.e., namely the 'surface area dissipation', but also from the redistribution of locked-in stored (strain) energy in the surrounding particles; the latter appears much larger in magnitude. Therefore, experimental deductions using measurements of energy changes through BET surface area (Brunauer *et al.*, 1934) may not represent the entire dissipation from grain crushing, as they miss the contribution from energy redistribution. We wish to clarify, however, that this does not mean that surface area creation is not important. On the contrary, without liberating the surface area (and freeing surface energy), the other component can not be activated, i.e., dissipation from energy redistribution. Therefore, a more significant dissipation ratio would be between the breakage (i.e., not only the surface area) dissipation and the frictional dissipation. It is important to note that while the surface area dissipation does not principally depend on the stress or strain paths, the breakage dissipation does, since it also involves the redistribution of the strain energy (which is path-dependent).

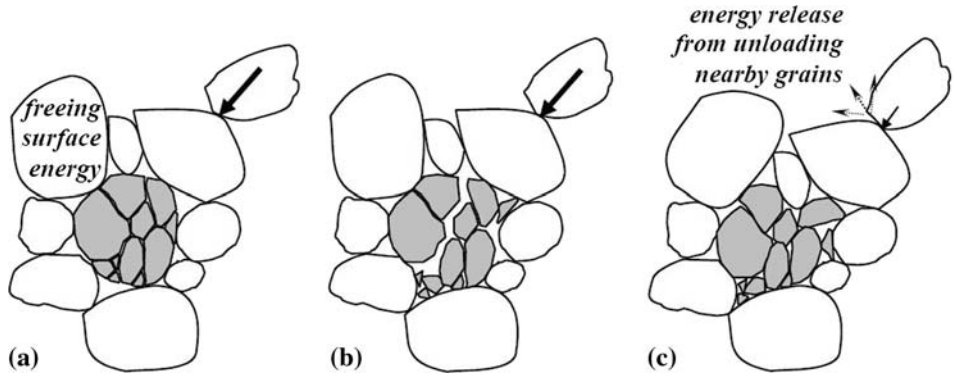

Figure 9

The dissipative events following the split of a particle. (a) new surface area is suddenly liberated, freeing surface energy; (b) the particle is replaced by fragments; (c) reorganisation of the fragments and their neighbours, leading to volumetric plastic dissipation (changes to configurational granular entropy) and dissipation from release of stored energy (Appendix) in nearby particles.

Therefore, for completion, it is important to study the dissipation ratio in relation to the load path. Finally, we remind that the overall dissipation in Eq. (11) includes not only the breakage dissipation and the frictional shear dissipation, but also the dissipation from the reorganisation of the surrounding particles, effectively represented by the plastic volumetric dissipation of Eq. (13).

5.1. Energy Balance Equation

The triaxial model described in Section 2 will be used as a basis for the following investigation. For isothermal processes (i.e., ignoring thermal temperature changes at this stage), the energy balance equation in incremental form is given as (ZIEGLER, 1983):

$$\tilde{W} = \delta\Psi + \tilde{\Phi}, \tag{43}$$

where $\tilde{W}$ is the rate of mechanical work input, and Ψ and $\tilde{\Phi}$ are the stored energy and dissipation potentials defined in Section 2. The tilde symbol $\sim$ is used here to highlight that the stored energy potential Ψ has a proper differential and is path-independent, while the other energy quantities are path-dependent and therefore only their rates can be defined, as $\tilde{W}$ and $\tilde{\Phi}$. Integration of this incremental equation over time results in the following energy balance equation in total form:

$$\Delta W = \Delta\Psi + \Delta\Phi \tag{44}$$

although we should highlight again the path-dependency of the first and third terms (i.e., not proper potentials). The total dissipated energy from a gouge element during the course of an earthquake is denoted here as $\Delta\Phi$, and the earthquake energy budget as the cumulative work ΔW.

While the overall dissipation involves three coupled mechanisms, as captured by Eq. (11), it may still be represented by three additive components (Einav, 2007b), corresponding to the breakage, particles reorganisation and frictional shear:

$$\Delta\Phi(t) = \int_0^t E_B\dot{B}dt + \int_0^t p\dot{\varepsilon}_v^p dt + \int_0^t q\dot{\varepsilon}_s^p dt = \Delta\Phi_{surface} + \Delta\Phi_{redist} + \Delta\Phi_{frict}. \tag{45}$$

However it should be noted that the strong coupling (Einav, 2007b) enforces the connection of these three additive components through the intrinsic dependence of E_B, p, and q on each other and also on δB, $\delta\varepsilon_v^p$, and $\delta\varepsilon_s^p$, besides their interaction through the constitutive equations. Based on the development in section 2, we can work out the ratio between the increments of energy dissipations:

$$\frac{E_B\delta B}{q\delta\varepsilon_s^p} = \frac{1}{2}\left(\frac{M^2}{\eta^2} - 1\right). \tag{46}$$

Although this is not the ratio between the total dissipations, it hints at the effect of loading path on the dissipation, through the stress ratio η between triaxial shear stress q and pressure p.

Furthermore, note that because the coupling angle in the current model is taken by $\omega = 45^\circ$, the energy losses from the breakage and the reorganization, through plastic volumetric strain, are equal for the sake of simplicity

$$p\delta\varepsilon_v^p = E_B\delta B. \tag{47}$$

In the current study, we focus on the dissipation ratio between the cumulative breakage and frictional shear terms, which is given as:

$$\text{dissipation ratio} = \frac{\int_0^t E_B\dot{B}\,\delta t}{\int_0^t q\dot{\varepsilon}_s^p\,\delta t} = \frac{\int_0^{B_t} E_B\delta B}{\int_0^{\varepsilon_{st}^p} q\,\delta\varepsilon_s^p}. \tag{48}$$

The above indicates the time-dependence of the dissipation ratio during the course of an earthquake.

5.2. *Numerical Approach to the Earthquake Energy Balance*

Numerical simulations are used here to explore the dissipation ratio. We consider four factors:

- initial stress state: through the ratio p_0/q_0, represented by the angle φ_0 (Fig. 10);
- the index property ϑ: measuring how far the initial *gsd* is from the ultimate *gsd*;
- trends of loading paths: through the loading angle φ (Fig. 10); and
- shear strain levels ε_s: the signature of a slip event.

The relative movement of the fault planes changes the triaxial stresses, initially represented here via the loading angle φ, with $\tan\varphi = \delta q/\delta p$. This presents only the

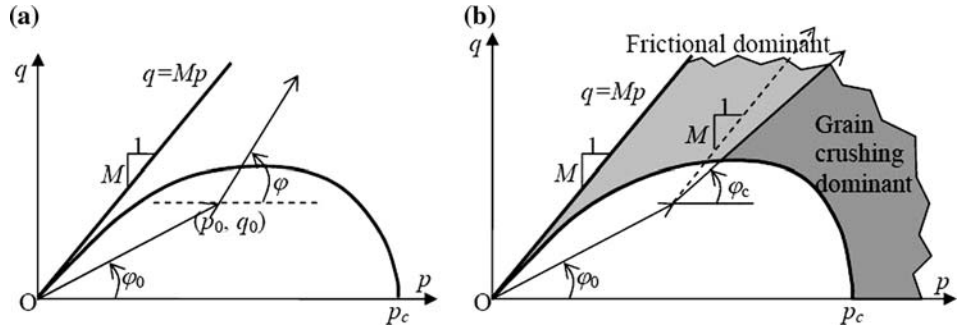

Figure 10
Schematic representation of loading trend during the course of an earthquake. (a): loading trend; (b): effect of loading trends on the dissipation.

trend of the loading during the course of an earthquake (Fig. 10). We note that the stress path depends on the far-field boundary conditions and the position of the granular element within the fault gouge, similar to those points that exist out of the gouge (Templeton and Rice, 2008). Both models 1 and 2 (see Section 2) are used here, with the following elasticity parameters: Young modulus $E = 70000$ MPa, Poisson's ratio $\nu = 0.15$ (Model 1); and $\bar{K} = \bar{G} = 255150$ (Model 2). Other parameters governing the inelastic response of the model are the same: crushing pressure $p_c = 300$ MPa, $M = 1.5$, $\vartheta = 0.5 \div 0.99$. The higher values of ϑ indicates a substantial "distance" between the initial and ultimate *gsd*'s, as experimentally observed in Reches and Dewers (2005). Other parameters in the parametric study are: initial pressure $p_0 = 30$ MPa, $\varphi = 0 \div \pi$, $\varphi_0 \approx 27°$ and 50°. The time at which all dissipated energies are measured is set for a cumulative shear strain of $\varepsilon_s^{\max} = 20$. In all numerical simulations, we get $B \approx 1$ at the final strain value of $\varepsilon_s^{\max} = 20$.

The breakage energy is higher than the frictional dissipation when φ is below a critical value φ_c determined as follows. For loading angle φ small enough, e.g., $\varphi < \text{atan}(M)$, the pressure p is very high at $\varepsilon_s = \varepsilon_s^{\max}$. In such cases the effect of the initial value $\eta_0 = q_0/p_0$ disappears. Therefore:

$$\tan\varphi = \frac{\delta q}{\delta p} \approx \frac{q|_{\text{at } \varepsilon_s^{\max}}}{p|_{\text{at } \varepsilon_s^{\max}}} = \eta|_{\text{at } \varepsilon_s^{\max}}. \tag{49}$$

From (46) and (48), the dissipation ratio has an upper bound (for $\varphi < \text{atan}(M)$):

$$\text{dissipation ratio} < \frac{1}{2}\left(\frac{M^2}{\left(\eta|_{\text{at } \varepsilon_s^{\max}}\right)^2} - 1\right) \approx \frac{1}{2}\left(\frac{M^2}{\tan^2\varphi} - 1\right). \tag{50}$$

This upper bound is independent of the index property ϑ, initial stress state represented by the angle φ_0, and even the elasticity model used. The numerical results in

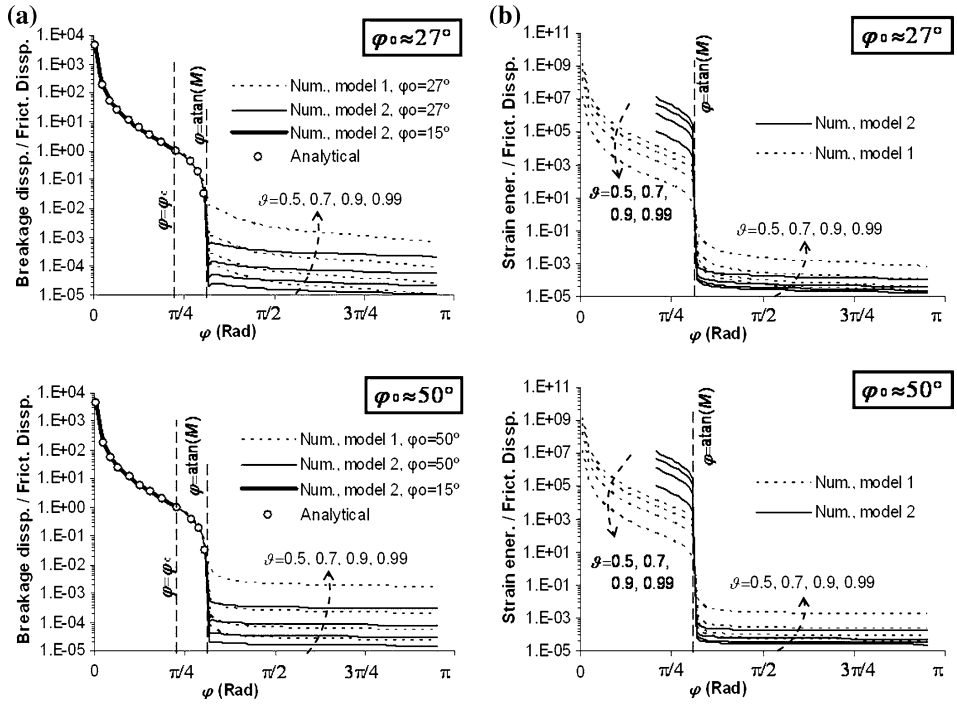

Figure 11
Effects of loading angle φ, initial stress state φ_0 and index property ϑ (using the constraint $\delta q/\delta p = \tan\varphi$). (a): on dissipation ratio; (b): on stored energy against friction dissipation.

Figure 11 confirm the above analytical approximation, which almost coincide with the dissipation ratio for $\varphi < \text{atan}(M)$.

From Eq. (50), for equal breakage and frictional shear dissipations we have $\eta = M/\sqrt{3}$, which results in an estimate for the critical angle φ_c separating frictional dominant and grain crushing dominant regimes (Fig. 10): $\varphi_c \approx \text{atan}\left(M/\sqrt{3}\right)$. In such cases, the critical state line can never be reached and the ratio between the breakage and frictional dissipation keeps increasing during the course of an earthquake. In addition, the elastic strain energy stored in the fault gouge material is also high (Fig. 11b), due to the confinement conditions.

The model behaviour under the constraint $\delta q/\delta p = \tan\varphi$ can result in different stress paths: either $\delta p > 0$ and $\delta q > 0$ (negative stress path) or $\delta p > 0$ and $\delta q > 0$ (positive stress path), depending on the initial stress state φ_0. For the pressure-dependent model, coupling terms in the constitutive equations (Eq. 30) affect the model responses under the constraint $\delta q/\delta p = \tan\varphi$. Therefore shearing too much (through high initial angle φ_0), and then reducing the shearing rate (through low loading angle φ) results in the model following negative stress path to conform with the enforced constraint. Since the effect of initial angle φ_0 on the energy balance under high pressure (e.g., for $\varphi < \text{atan}(M)$) is

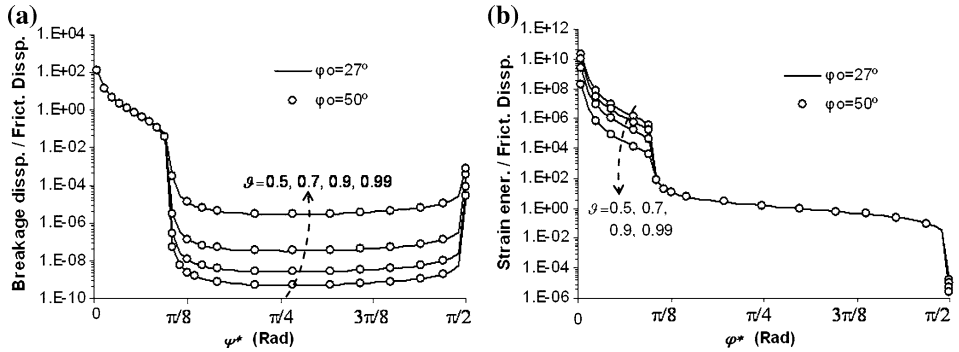

Figure 12

Effects of loading angle φ^* (in strain space), initial stress state φ_0 and index property ϑ (using the constraint $\delta\varepsilon_s/\delta\varepsilon_v = \tan\varphi^*$ in strain space). (a): on dissipation ratio; (b): on stored energy against friction dissipation.

negligible (Fig. 11a, and Eq. (50)) $\varphi_0 = 15°$ was used to complete the energy balance curve for the pressure-dependent model (Fig. 11a). To complement the results obtained in stress space, loading paths with constraint $\delta\varepsilon_s/\delta\varepsilon_v = \tan\varphi^*$ in strain space were also used, resulting in only negligible difference for two different initial states with $\varphi_0 \approx 27°$ and $\varphi_0 \approx 50°$ (Fig. 12).

The initial states of the material seem to have only marginal effects on the way the earthquake energy is dissipated, as seen in Figures 11 and 12. The dissipation ratio and the ratio between the stored energy against the friction dissipation, for the varying initial states ($\varphi_0 = 27°$ and $\varphi_0 = 50°$), do not show significant difference. Conversely, the index property ϑ has a major effect on the dissipation ratios only when $\varphi > \text{atan}(M)$. Below that, it is mainly governed by the loading path (Fig. 11). Similar conclusions can be withdrawn for the ratio between the stored strain energy Ψ and the frictional dissipation, except the fact that the index property ϑ has effects on this ratio in the entire range of loading angles φ (Fig. 11b).

The effects of shear-strain levels on the dissipative processes can be seen in Figure 13. For load paths with low loading angles φ (in grain crushing dominant regime; Fig. 10) the effects of shear-strain level on the dissipation ratio are negligible. In such cases, regardless of the amount of shear or to what extent the *gsd* progresses, the breakage energy always dominates the earthquake energy budget. For φ higher than the critical angle φ_c, the dissipation ratio decreases with increasing shear-strain level, indicating that frictional shear dissipation is the dominant dissipation mechanism.

Based on the above numerical investigation, we conclude that the loading trend, which governs the stress field (e.g., shear-dominant or compression-dominant), has the most important effect on the consumption of the energy budget. If the material is subjected to compression-dominant stress fields, we find that the crushing of rock grains (including both the creation of new surface area and release of locked-in strain energy) consumes most of the energy budget. It is noted that these results are subjected to the

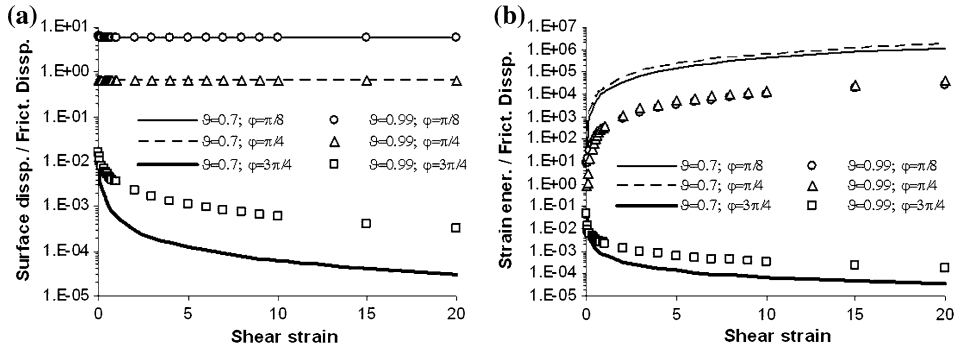

Figure 13
Effects of shear strain levels. (a): On dissipation ratio; (b): on stored energy against friction dissipation.

condition that the *gsd* at the end of the faulting process has reached its ultimate state, characterized in the analysis by breakage variable B reaching one. This reflects a state at which the cataclastic flow occurs without further grain crushing. Therefore, conclusions based on experimental analysis of cataclasite material, that the surface area dissipation can account for 50% or more of the earthquake energy, should be carefully examined (ROCKWELL *et al.*, 2008).

We note that the surface area dissipation is only the smaller component of the breakage dissipation (see the Appendix); the other bigger component, indirectly related to the production of new surface, is the energy release from the redistribution of locked-in strain energy in the surrounding grains. In shear-dominant faults, we find that the sum of these two crushing dissipation terms (giving the breakage dissipation) is negligible compared to the frictional dissipation, which dominates the earthquake energy budget. This in agreement with the common observations related to fault zone environments (e.g., in OLGAARD and BRACE, 1983; CHESTER *et al.*, 2005; and ROCKWELL *et al.*, 2008).

6. Conclusions

We studied several aspects of faulting using a breakage mechanics constitutive model, with only four physically identifiable parameters. The intrinsic capability of the model to predict the aspect of evolving *gsd* opens up opportunities in characterising well both the mechanical responses and permeability reduction of rocks during cataclasis events. Our study highlighted the importance of understanding the various elements of energy dissipation mechanisms for studying fault gouge energetics. In particular, the total energy dissipation from crushing of a confined granular ensemble, modelled here using the breakage energy dissipation, was found to contain both the surface area dissipation and the redistribution of locked-in strain energy. This understanding raises a question

regarding the relevance of the BET surface area (Brunauer *et al.*, 1938) for quantifying the energy released during an confined pulverization, since the redistribution of locked-in strain energy is more prominent compared to the surface area dissipation. Based on this finding, the issue of energy balance in fault zones during an earthquake was tackled differently from previous research. The consumption of earthquake energy budget was found to depend mostly on a loading path governed by the relative movement of fault planes, resulting in different scenarios of the energy balance.

Acknowledgements

The authors would like to express their gratitude to Professor Teng-fong Wong (State University of New York) for the permission to use his experimental data on sandstones. The supply of experimental data on Cambria sand from Professor Poul Lade (The Catholic University of America), although not used in the paper, is also acknowledged. This research was supported under the Australian Research Council's *Discovery Projects* funding scheme (project number DP0774006).

Appendix: Mechanical Analog of Breakage Dissipation

A simple mechanical analog is set up here to illustrate the conceptual difference between the surface area dissipation, i.e., the part which relates linearly to changes in BET surface area (Brunauer *et al.*, 1938), and the breakage dissipation in breakage mechanics. Two sets of particle blocks are stacked alongside in a one-dimensional configuration, separated by a single particle (blackened in Fig. A1). For simplicity we assume that each of the separated sets contains a similar number of particles, each having a stiffness K_p. The particle that separates between these packs, i.e., the blackened particle, is assumed to be fully rigid but connected via two flexible bonds to the ground. The bond stiffness is assumed to be $K_b = aK_p$. Given N equally long particles in each of the blocks, with each particle having a length l, a single particle block has the stiffness $K = K_p/N$ and length $L = Nl$. The result is that the overall combined stiffness of the system is initially given by:

$$\bar{K} = \frac{(1 + 2aN)}{2aN(1 + aN)} K_b. \tag{A1}$$

This suggests that as the number of particles (N) in a stack is assumed sufficiently large, the overall stiffness becomes much smaller compared to the bond stiffness K_b (for a finite coefficient a).

The characteristic number N of the particle blocks in a stack can be seen as the number of particles in natural granular agglomerates that transmit a single force chain, with a mean value $N = 5 \div 6$ (Muthuswamy and Tordesillas, 2006). The characteristic

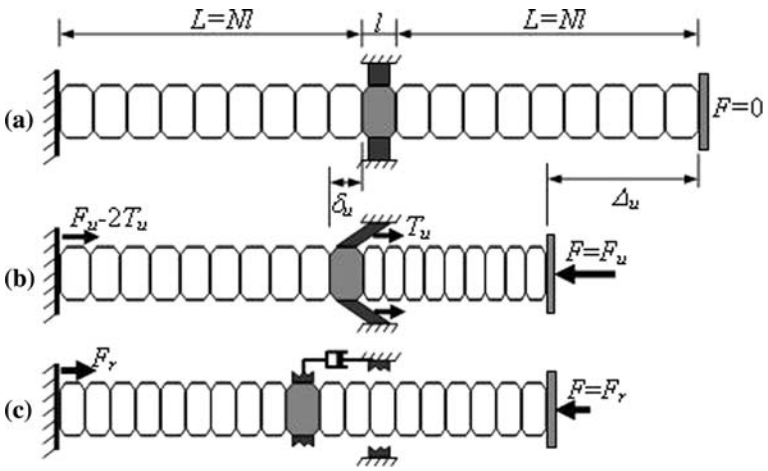

Figure A1
Mechanical analog: (a) initial configuration; (b) ultimate state; (c) bond breaking → release of locked-in strain energy and stress redistribution. The damper is shown only in (c), as it is irrelevant in (a) and (b) during quasi-static loading.

length of a particle block in the analog may be taken at the order of a harmonic grain diameter D_H in the natural agglomerate, since the analog sets grain blocks in a series. Finally, the coefficient a is of the order of one, to allow seeing the analog bonds as representative of a crushable particle.

We start to load the analog, under sufficiently slow displacement controlled conditions, to eliminate dynamic damping effects before the bonds open up. The whole system of particle blocks and bonds compress, as shown in Figure A1-b. When the bonds reach their ultimate shear force capacity T_u, and their ultimate elastic slip δ_u (see inset in Fig. A2), the system reaches an ultimate state represented by $F = F_u$ and $\Delta = \Delta_u$ (see Fig. A2), where $\Delta \ll L$ for small strain deformations. Right before the opening of the bonds at the ultimate state, the total elastic strain energy in the system, denoted here as Ψ_u, is:

$$\Psi_u = \frac{K}{2}(\Delta_u - \delta_u)^2 + K_b\delta_u^2 + \frac{K}{2}\delta_u^2. \tag{A2}$$

The bond breaking is abrupt (Fig. A2), and therefore the elastically stored energy in the bonds ($K_b\delta_u^2$= double the shaded areas in Fig. A2) is totally released for the creation of surface area:

$$\Delta\Phi_{\text{surface}} = K_b\delta_u^2. \tag{A3}$$

On the other hand, at this point the overall displacement freezes at $\Delta = \Delta_u$, which represents the confining condition of the granular ensemble. However, the force F fluctuates around an equilibrium force F_r, with a velocity that can no longer be

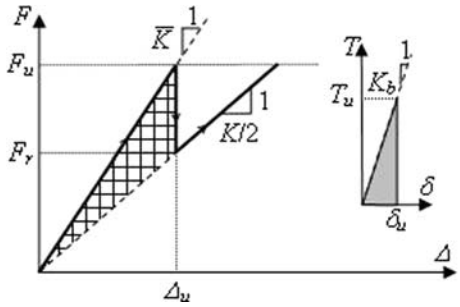

Figure A2
Load-displacement curves of the system response (hatched area designates the overall breakage dissipation, including both surface area dissipation and dissipation from redistribution of locked-in strain energy). Inset picture shows the response of an individual breakable bond (in this case the shaded area designates only the surface area dissipation of a single bond).

considered negligible. Therefore, the notional damper, shown in Figure A1-c, is activated for the first time, providing an additional reaction against the motion of the rigid particle, until this gets into static equilibrium and the force fluctuations are eliminated, i.e., when $F = F_r$. In analogy with natural agglomerates, the damper reflects heat production.

After the oscillations stop (which could notionally be considered quite rapidly, given a sufficiently large damping coefficient[1]), the system could again be seen in a quasi-static condition and the loading is still under an overall displacement $\Delta = \Delta_u$. In other words, the system travels along the minimum of the global potential energy. As a consequence, during the entire dynamic equalisation towards the static equilibrium condition, the change in the mechanical work input could be considered zero $\Delta W = 0$, and the elastically stored energy in the system at static equilibrium condition can be worked out:

$$\Psi_r = \frac{K}{4}\Delta_u^2. \tag{A4}$$

Recalling now the energy balance equation in thermodynamics (Eq. (44)):

$$\Delta\Phi = \Delta W - \Delta\Psi, \tag{A5}$$

the energy dissipation is:

$$\Delta\Phi = -\Delta\Psi = \Psi_u - \Psi_r = K_b\delta_u^2 + \frac{K_b}{K}K_b\delta_u^2 = \Delta\Phi_{\text{surface}}\left(1 + \frac{K_b}{K}\right). \tag{A6}$$

In other words, we find that in this analog the total dissipation is the sum of two dissipation terms:

[1] as found useful for simulating quasi-static loading of granular assemblies using the discrete element method (Cundall and Strack, 1979).

$$\Delta\Phi = \Delta\Phi_{\text{surface}} + \Delta\Phi_{\text{redist}}, \tag{A7}$$

where we designate the dissipation from the redistribution of initially locked-in strain energy:

$$\Delta\Phi_{\text{redist}} = aN\Delta\Phi_{\text{surface}} \tag{A8}$$

recalling that $K_b = aK_p$ and $K = K_p/N$.

For a growing number of particles N in the block, $\Delta\Phi_{\text{redist}} \gg > \Delta\Phi_{\text{surface}}$, since a is in the order of one. As can be seen via eq. (A7), the total energy dissipation (hatched area in Fig. A2) contains both the dissipation from the creation of new surface area (shaded area in inset, Fig. A2), and the dissipation from the redistribution of the locked-in strain energy.

Note that in this example the total dissipation $\Delta\Phi$ depends only on the difference between two (static) equilibrium states of the system before and after the bond breaking process. Independently from the details that define the dynamics during the intermediate process, i.e., the choice of the damping coefficient, the total mechanical dissipation $\Delta\Phi$ remains unchanged and can be readily worked out from the difference between minimum potential energies in static states before and after the breaking of bonds. Therefore the notional damper illustrates that the release of "locked-in strain energy" goes to the production of heat.

The above analysis shows that under confining conditions there is a fundamental difference between the breakage energy dissipation and the surface area dissipation. It is the entire breakage energy dissipation which was shown to be primarily related to the redistribution of locked-in strain energy, and not only the surface area dissipation, that represents the grain crushing. Therefore, estimates of dissipation energetics in cataclasis must account for the path dependency of the material behaviour, in addition to measurements of BET surface area. However, we note that in shear-dominant faults, our analysis in the main body of the paper shows that the sum of these two crushing dissipation terms (giving the breakage dissipation) is negligible compared to the frictional dissipation, which dominates the earthquake energy budget. This is in agreement with the common observations related to fault zone environments (e.g., in Olgaard and Brace, 1983; Chester *et al.*, 2005; and Rockwell *et al.*, 2008).

References

An, L.-J. and Sammis, C.G. (1994), *Particle size distribution of cataclastic fault materials from Southern California: A 3-D study*, Pure Appl. Geophys. *143*(1), 203–227.

Aydin, A., Borja, R.I., and Eichhubl, P. (2006), *Geological and mathematical framework for failure modes in granular rock*, J. Struct. Geol. *28*(1), 83–98.

Beeler, N.M., Tullis, T.E., Blanpied, M.L., and Weeks, J.D. (1996), *Frictional behavior of large displacement experimental faults*, J. Geophys. Res. *101*(B4), 8697–8715.

Ben-Zion, Y. (2008), *Collective behavior of earthquakes and faults: Continuum-discrete transitions, progressive evolutionary changes and different dynamic regimes*, Rev. Geophys. *46*, RG4006, doi:10.1029/2008RG000260.

Ben-Zion, Y. and Sammis, C.G. (2003), *Characterization of fault zones*, Pure Appl. Geophys. *160*(3), 677–715.

Borja, R.I., Tamagnini, C., and Amorosi, A. (1997), *Coupling plasticity and energy-conserving elasticity models for clays*, J. Geotech. Geoenviron. Engin. *123*(10), 948–957.

Brunauer, S., Emmett, P.H., and Teller, E. (1938), *Adsorption of gases in multimolecular layers*, J. Am. Chem. Soc. *60*(2), 309–319.

Caine, J.S., Evans, J.P. and Forster, C.B. (1996), *Fault zone architecture and permeability structure*, Geology *24*(11), 1025–1028.

Chester, J.S., Chester, F.M., and Kronenberg, A.K. (2005), *Fracture surface energy of the Punchbowl fault, San Andreas system*, Nature *437*(7055), 133–136.

Cundall, P. and Strack, O. (1979), *A discrete numerical model for granular assemblies*, Geotechnique *29*, 47–65.

Cuss, R.J., Rutter, E.H. and Holloway, R.F. (2003), *The application of critical state soil mechanics to the mechanical behaviour of porous sandstones*, Internat. J. Rock Mech. and Mining Sci. *40*, 847–862.

Edwards, S.F. and Grinev, D.V. (2001), *Transmission of stress in granular materials as a problem of statistical mechanics*, Physica A *302*, 162–186

Einav, I. (2007a), *Breakage mechanics–Part I: Theory*, J. Mechan. Phys. Sol. *55*(6), 1274–1297.

Einav, I. (2007b), *Breakage mechanics–Part II: Modelling granular materials*, J. Mech. Phys. Sol. *55*(6), 1298–1320.

Einav, I. (2007c), *Fracture propagation in brittle granular matter*, Proc. Roy. Soc. A: Math., Phys. Eng. Sci. *463*(2087), 3021–3035.

Einav, I. (2007d), *Soil mechanics: breaking ground*, Philosoph. Transac. Roy. Soc. A: Math., Phys. Engin. Sci. *365*(1861), 2985–3002.

Einav, I., Vardoulakis, I., and Chan, A.H.C. (2008), *Confined comminution and permeability reduction in expanding perforations*, to be submitted.

Einav, I. and Puzrin, A.M. (2004), *Pressure-dependent elasticity and energy conservation in elastoplastic models for soils*, J. Geotechn. Geoenviron. Engin. *130*(1), 81–92.

Evans, J.P., Forster, C.B., and Goddard, J.V. (1997), *Permeability of fault-related rocks, and implications for hydraulic structure of fault zones*, J. Struct. Geol. *19*(11), 1393–1404.

Griffith, A.A. (1921), *The phenomena of rupture and flow in solids*, Philosoph. Transact. Roy. Soc. London. Series A, Containing Papers of a Math. or Phys. Character (1896–1934) 221(-1), 163–198.

Guo, Y. and Morgan, J.K. (2007), *Fault gouge evolution and its dependence on normal stress and rock strength—Results of discrete element simulations: Gouge zone properties*, J. Geophys. Res. *112*(B10403), 1–17.

Hamiel, Y., Lyakhovsky, V., and Agnon, A. (2004), *Coupled evolution of damage and porosity in poroelastic media: theory and applications to deformation of porous rocks*, Geophys. J. Internatl. *156*, 701–713

Heilbronner, R. and Keulen, N. (2006), *Grain size and grain shape analysis of fault rocks*, Tectonophysics *427*(1–4), 199–216.

Hoque, E. and Tatsuoka, F. (1998), *Anisotropy in elastic deformation of granular materials*, Soils Found. *38*(1), 163–179.

Houlsby, G.T. (1985), *The use of a variable shear modulus in elastic-plastic models for clays*, Comp. Geotechn. *1*(1), 3–13.

Houlsby, G.T., Amorosi, A., and Rojas, E. (2005), *Elastic moduli of soils dependent on pressure: A hyperelastic formulation*, Geotechnique *55*(5), 383–392.

Kendall, K. (1978), *The impossibility of comminuting small particles by compression*, Nature *272*, 710–711.

LoPresti, D.C.F. and O'Neill, D.A. (1991), *Laboratory investigation of small strain modulus anisotropy in sands*, Proc. ISOCCTI, Clarkson University, Potsdam, 1991, pp. 213–224.

Lund, M.G. and Austrheim, H. (2003), *High-pressure metamorphism and deep-crustal seismicity: Evidence from contemporaneous formation of pseudotachylytes and eclogite facies coronas*, Tectonophysics *372*(1–2), 59–83.

Lyakhovsky, V., Ben-Zion, Y., and Agnon, A. (1997), *Distributed damage, faulting, and friction*, J. Geophys. Res. *102*(B12), 27,635–27,649.

Mandl, G., de Jong, L.N.J., and Maltha, A. (1977), *Shear zones in granular material*, Rock Mech. Rock Engin. *9*(2), 95–144.

MARONE, C., RALEIGH, C.B., and SCHOLZ, C.H. (1990), *Frictional behavior and constitutive modeling of simulated fault gouge*, J. Geophys. Res. *95*(B5), 7007–7025.

MARONE, C., VIDALE, J.E., and ELLSWORTH, W.L. (1995), *Fault healing inferred from time-dependent variations in source properties of repeating earthquakes*, Geophys. Res. Lett. *22*(22), 3095–3098.

MATYKA, M., KHALILI, A., and KOZA, Z. (2008), *Tortuosity-porosity relation in porous media flow*, Phys. Rev. E *78*, 026306.

MCGARR, A., FLETCHER, J.B., and BEELER, N.M. (2004), *Attempting to bridge the gap between laboratory and seismic estimates of fracture energy*, Geophys. Res. Lett. *31*, L14606.

MORROW, C., SHI, L.Q., and BYERLEE, J. (1981), *Permeability and strength of San Andreas fault gouge under high pressure*, Geophys. Res. Lett. *8*(4), 325–328.

MUTHUSWAMY, M. and TORDESILLAS, A. (2006), *How do interparticle contact friction, packing density and degree of polydispersity affect force propagation in particulate assemblies*?, J. Stat. Mech. - Theory and Experiment, P09003.

OKADA, Y., SASSA, K., and FUKUOKA, H. (2004), *Excess pore pressure and grain crushing of sands by means of undrained and naturally drained ring-shear tests*, Engin. Geol. *75*(3–4), 325–343.

OLGAARD, D.L. and BRACE, W.F. (1983), *The microstructure of gouge from a mining-induced seismic shear zone*, Internatl. J. Rock Mechan. and Mining Sci. Geomechan. Abstracts 20(1), 11–19.

OLSEN, M.P., SCHOLZ, C.H., and LÉGER, A. (1998), *Healing and sealing of a simulated fault gouge under hydrothermal conditions: Implications for fault healing*, J. Geophys. Res. *103*(B4), 7421–7430.

OLSSON, W.A. (1999), *Theoretical and experimental investigation of compaction bands in porous rock*, J. Geophys. Res. *104*(B4), 7219–7228.

PITTARELLO, L., DI TORO, G., BIZZARRI, A., PENNACCHIONI, G., HADIZADEH, J. and COCCO, M. (2008), *Energy partitioning during seismic slip in pseudotachylyte-bearing faults (Gole Larghe Fault, Adamello, Italy)*, Earth Planet. Sci. Lett. *269*(1–2), 131–139.

RECHES, Z. and DEWERS, T.A. (2005), *Gouge formation by dynamic pulverization during earthquake rupture*, Earth Planet. Sci. Lett. *235*(1-2), 361–374.

RENARD, F., GRATIER, J.-P., and JAMTVEIT, B. (2000), *Kinetics of crack-sealing, intergranular pressure solution, and compaction around active faults*, J. Struct. Geol. *22*(10), 1395–1407.

RICARD, Y. and BERCOVICI, D. (2003), *Two-phase damage theory and crustal rock failure: The theoretical 'void' limit, and the prediction of experimental data*, Geophys. J. Internatil. *155*, 1057–1064.

RICE, J.R. (1978), *Thermodynamics of the quasi-static growth of Griffith cracks*, J. Mechan. Phys. Sol. *26*, 61–78.

ROCKWELL, T., SISK, M., GIRTY, G., DOR, O., WECHSLER, N., and BEN-ZION, Y. (2009), *Chemical and physical characteristics of pulverized Tejon lookout Granite Adjacent to the San Andreas and Garlock faults: implications for earthquake physics*, Pure Appl. Geophys., in press.

ROSCOE, K.H. and SCHOFIELD, A.N. (1963), *Mechanical behaviour of an idealised 'wet' clay*, European Conf. Soil Mechan. Foundation Engin. Essen, Germany: Deutsche Gesellschaft für Erd- und Grundbau, E.v., Wiesbaden, 46–54.

SAMMIS, C.G. and BEN-ZION, Y. (2008), *Mechanics of grain-size reduction in fault zones*, J. Geophy. Res. *113*, B02306.

SAMMIS, C.G., OSBORNE, R.H., ANDERSON, J.L., BANERDT, M., and WHITE, P. (1986), *Self-similar cataclasis in the formation of fault gouge*, Pure Appl. Geophys. *124*(1), 53–78.

SCHOLZ, C. *The Mechanics of Earthquakes and Faulting* (Cambridge University Press 1990).

SCHULTZ, R.A. and SIDDHARTHAN, R. (2005), *A general framework for the occurrence and faulting of deformation bands in porous granular rocks*, Tectonophysics *411*(1–4), 1–18.

SEGALL, P. and RICE, J.R. (1995), *Dilatancy, compaction, and slip instability of a fluid-infiltrated fault*, J. Geophys. Res. *100*(B11), 22,155–122,171.

SHAH, K.R. (1997), *An elasto-plastic constitutive model for brittle-ductile transition in porous rocks*, Internatl. J. Rock Mechan. Mining Sci. *34*(3–4), 283.e281–283.e213.

SHELDON, H.A., BARNICOAT, A.C., and ORD, A., (2006), *Numerical modelling of faulting and fluid flow in porous rocks: An approach based on critical state soil mechanics*, J. Struct. Geol. *28*(8), 1468–1482.

SHI, Z., BEN-ZION, Y. and NEEDLEMAN, A. (2008), *Properties of dynamic rupture and energy partition in a solid with a frictional interface*, J. Mechan. Phys. Sol. *56*, 5–24.

Sleep, N.H. and Blanpied, M.L. (1992), *Creep, compaction and the weak rheology of major faults*, Nature *359*(6397), 687–692.

Steacy, S.J. and Sammis, C.G. (1991), *An automaton for fractal patterns of fragmentation*, Nature *353*(6341), 250–252.

Templeton, E.L. and Rice, J.R., (2008), *Off-fault plasticity and earthquake rupture dynamics, 1. Dry materials or neglect of fluid pressure changes*, J. Geophys. Res. B (Solid Earth), *113*, B09306, doi:10.1029/2007JB005529.

Tenthorey, E., Cox, S.F., and Todd, H.F. (2003), *Evolution of strength recovery and permeability during fluid-rock reaction in experimental fault zones*, Earth Planet. Sci. Lett. *206*(1–2), 161–172.

Wilson, B., Dewers, T., Reches, Z.E. and Brune, J. (2005), *Particle size and energetics of gouge from earthquake rupture zones*, Nature *434*(7034), 749–752.

Wong, T., David, C., and Zhu, W. (1997), *The transition from brittle faulting to cataclastic flow in porous sandstones: Mechanical deformation*, J. Geophys. Res. *102*(B2), 3009–3025.

Xia, K. (2006), *Scaling of fracture energies: The rationalization of different laboratory measurements*, Geophys. Res. Lett. *33*, L01305.

Zhang, S. and Tullis, T.E. (1998), *The effect of fault slip on permeability and permeability anisotropy in quartz gouge*, Tectonophysics *295*(1–2), 41–52.

Zhu, W. and Wong, T. (1997), *The transition from brittle faulting to cataclastic flow: Permeability evolution*, J. Geophys. Res. *102*(B2), 3027–3041.

Ziegler, H. *An introduction to thermomechanics*, Second Ed. (North Holland, Amsterdam 1983).

Zytynski, M., Randolph, M.F., Nova, R. and Wroth, C.P. (1978), *On modelling the unloading-reloading behaviour of soils*, Internatl. J. Numer. Analyt. Methods in Geomechan. *2*(1), 87–93.

(Received August 1, 2008, accepted January 10, 2009)